Heliyon 9 (2023) e16198

Contents lists available at ScienceDirect

Heliyon

journal homepage: www.cell.com/heliyon

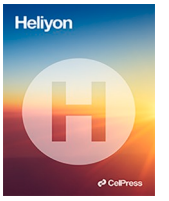

Research article

The theoretical model and sinusoidal optimization strategy for oscillating shear valve type continuous waves generator

Liang Xue, Hu Han *, Yaoyao Shen, Lewang Sun, Honghai Fan

College of Petroleum Engineering, China University of Petroleum, Beijing, 102249, China

ARTICLE INFO

Keywords:
Continuous-wave mud pulse
Oscillating shear valve tool
Sine wave
Pressure drop
Optimization strategy
CFD

ABSTRACT

Continuous-wave mud generator is widely adopted for real-time downhole data transmission of deep wells in the oil industry. There have been many studies on rotor structure optimization of continuous rotary valve tools but few studies on the different optimization mechanisms of oscillating shear valve tools. In this paper, a theoretical model of pressure wave generation for oscillating shear valve tools was presented, and the reason for the non-sinusoidal waveform was analyzed theoretically for the first time. A series of rotor rotation strategies were proposed to improve the sinusoidal properties of pressure waves without changing the mechanical structure of the rotor. Finally, CFD with different parameters was conducted to verify the feasibility of the optimization scheme. The numerical results give the recommended range of parameters under different control schemes. In addition, the relationship between throttle pressure drop and pressure wave waveform is found through comparison with previous research of the team, which provides a new research idea for the optimization of the pressure wave in the future.

1. Introduction

With the development of ultradeep wells, downhole data information has rapidly increased at present, so logging while drilling (LWD) and measurement while drilling (MWD) require faster data transmission speed and stability [1,2]. The most commonly used wireless data transmission method is mud pulse telemetry (MPT), which has high reliability, low development cost, strong anti-interference, and the ability to transfer data quickly and efficiently in a wide variety of deep wells [3]. The mud pulse generator changes the flow area of the drilling mud to generate pressure waves and transmits downhole data to the surface after coding the downhole. The mud pulse can be divided into three main categories according to the type of valve: negative pulse, positive pulse, and continuous wave [4–7]. A negative pulse is generated when a portion of the drilling fluid is removed from the drill pipe by a reciprocating valve, creating a rapid pressure drop. The positive pulse plugs a portion of the drilling fluid through the reciprocating movement of a tapered valve mounted in the drill pipe, creating a localized pressure rise that generates the pressure wave [8]. As shown in Fig. 1, the data from downhole measurements are typically sent to the wellhead using a specific code modulated. After the data are encoded and modulated, the continuous wave pulse is controlled by a motor to rotate. The modulated signal pulse is transmitted through the drill pipe channel to the surface. Then, the signal is filtered and extracted on the surface, and the information transmitted downhole is decoded.

* Corresponding author.
E-mail addresses: xueliang200888@126.com (L. Xue), hancupb@126.com (H. Han), 1610886851@qq.com (Y. Shen), 13261088366@139.com (L. Sun), fanhh@cup.edu.cn (H. Fan).

https://doi.org/10.1016/j.heliyon.2023.e16198
Received 3 November 2022; Received in revised form 27 April 2023; Accepted 9 May 2023
Available online 25 May 2023

The core components of a continuous wave generator are a pair of rotors and stators, whose structure has the same valve blades. A motor drives the rotor, and continuous waves are generated with the discontinuous opening and closing of the stator and rotor. Different motor control methods determine the characteristics of continuous waves, which can currently reach frequencies of 6–40Hz [9]. Although the continuous wave pulse generator has been improved over the past few decades, the pressure wave p could be a better sine wave, which contains many high-energy harmonics. When pressure wave signals transmit long distances in the wellbore, the signal amplitude decays exponentially and is difficult to detect on the surface [10,11]. Therefore, many studies have eliminated harmonic components and generated ideal sine waves.

Continuous wave generators are mainly classified as continuous rotary valve types and oscillating shear valve types. The former generates a change in the flow area through continuous rotation of the rotor at a constant angular velocity. In contrast, the latter generates pressure waves through the reciprocating oscillating of the rotor at a small angle by changing the angular velocity [9]. Because the oscillating shear valve types valve can be rotated at a small angle, it is suitable for a variety of modulation modes. There are many rotations available compared to continuous valve types, so it is becoming a mainstream development direction for downhole mud puler tools. At present, waveform optimization methods refer to thin-wall throttling theory [12], and the pressure drop is defined as:

$$\Delta P = \frac{\rho_0 Q^2}{2C_d^2} * \frac{1}{S^2(t)} \tag{1}$$

where ρ_0 is the fluid density, kg/m^3; Q represents the displacement through the rotor, which is usually considered constant, m^3/s; C_d is the flow coefficient; and $S(t)$ denotes the flow area of the rotor during rotation, m^2.

Since the design goal is that the pressure difference is a sine function varying with time, it can be simplified as:

$$\Delta P = A\ \sin(\omega * t) + B \tag{2}$$

where ω is the angular velocity of rotor rotation, A and B are the maximum and minimum amplitudes, respectively.

Based on Eq. (1) and Eq. (2), it can be concluded that the reciprocal of the square of the area function must meet the sine function to obtain the sinusoidal pressure difference, that is

$$\sin(\omega * t) \sim \frac{1}{S^2(t)} = \frac{1}{f^2(\theta)} \tag{3}$$

where θ is the rotation angle of the stator, rad, and $f(\theta)$ represents the flow area as a function of θ.

Therefore, the optimization design methods of the two tools are completely different. First, the rotation angular velocity of the rotary valve generator is constant for the rotary valve generator, so the rotation angle is proportional to time. By integrating Eq. (3), the design goal becomes to design the flow area so that it is the sine function of θ, that is,

$$\frac{1}{S^2(t)} \sim \sin(\theta) \tag{4}$$

According to this design idea of Eq. (4), many scholars have carried out a series of theoretical derivations and designs of stator and rotor valve lines and have obtained perfect sine waves [13–21]. However, to ensure the incomplete closing of the flow channel between the stator and rotor, there are gaps and axial annular gap flow, so a mathematical model makes it very difficult to describe the flow situation directly. Therefore, many scholars have combined theoretical models and numerical methods to optimize the structure. Wang et al. numerically simulated the three-dimensional flow field of rotary valve type mud pulse generator. Yan et al. optimized valve

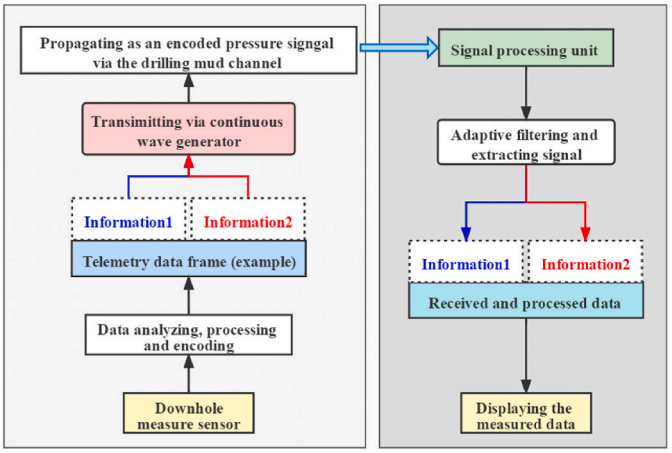

Fig. 1. The transmission process of the continuous wave MPT.

structures to achieve similar sinusoidal pressure signals, which was verified by computational fluid dynamics (CFD) simulations. We also integrated the CFD method and optimized and designed a sinusoidal pressure wave generator (SPWG) consistent with the ground test results.

There are many studies on the sinusoidal optimization of rotary valve tools, and excellent design results have been achieved. However, the optimization design method of the oscillating shear valve tool is more complicated. Most importantly, the rotor of the oscillating shear valve tool needs to be accelerated and decelerated periodically to achieve small-angle reciprocating motion. Meanwhile, the stator and rotor valve lines are designed to facilitate the design, and the flow area is proportional to the angle. Therefore, the design goal becomes to design how the rotor rotates, that is,

$$\frac{1}{[\omega(t) * t]^2} \sim \sin(\omega(t) * t) \tag{5}$$

where $\omega(t)$ is the rotation angular velocity of the rotor as a function of time.

Eq. (5) shows that the angular velocity change of the rotor determines the sinusoid of its waveform. However, there is little research on rotor control of oscillating shear valve tools.

With the development of MWD and LWD, the volume of downhole data is increasing, which requires the pulse tool to accommodate a variety of data modulation methods. Oscillating shear valve tools can be set according to the need for continuous rotation or oscillating mode of work and will be more widely used. However, the pressure waveform is nonsinusoidal, which is in urgent need of theoretical guidance for optimal design. Therefore, this study carries out theoretical research on this problem and adopts the CFD method to verify it.

The following sections of this paper are organized as follows. The principle of waveform optimization is proposed in Section 2, and the CFD simulation method is given in Section 3. Simulation results are provided and discussed in Section 4. Finally, the conclusions are elaborated in Section 5.

2. The principle of waveform optimization

2.1. Theoretical model of pressure wave calculation

The stator and rotor of the mud wave generator have the same radius, and the geometric structure of the rotor is shown in Fig. 2. The central angle of the rotor blade is 32°, and the blade spacing angle is 28°. R_0 is the outer diameter of the stator, R_1 is the outer diameter of the rotor. The annulus gap always produces an overcurrent because the stator is slightly larger than the rotor. Fig. 2 shows the coincident state of the rotor with stator, in which the flow area is the largest and is defined as S_0. The maximum flow area can be divided between the valves in the annulus flow area S_1 and flow area S_2.

These two areas can be obtained as follows:

$$S_1 = \pi\left(R_0^2 - R_1^2\right) \tag{6}$$

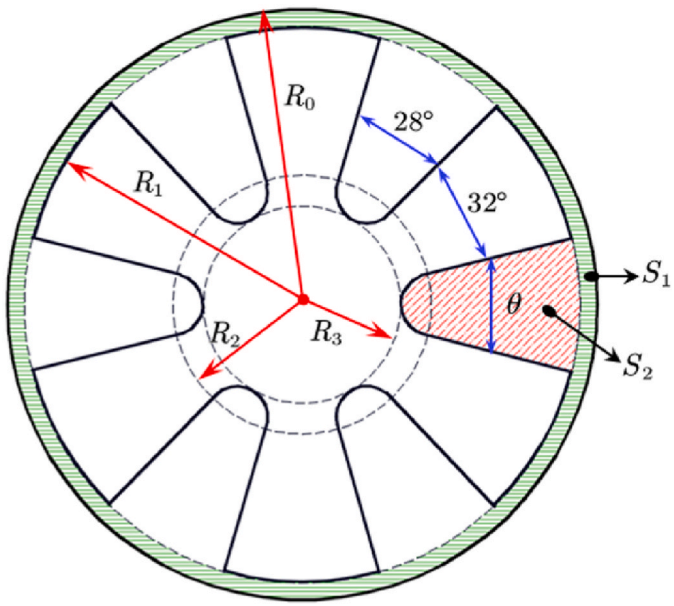

Fig. 2. Geometric model of a continuous wave generator rotor.

$$S_2 = \frac{\theta}{2}\left(R_0^2 - R_1^2\right) + \frac{\pi}{2}(R_2 - R_3)^2 \tag{7}$$

$$S_0 = S_1 + 6S_2 \tag{8}$$

where R_0 and R_1 denote the outer diameter of the stator and rotor, respectively, mm; R_3 and R_4 are the characteristic radius of the disc, mm; θ represents the radian between the rotor discs, rad.

The rotor rotates clockwise when a continuous wave generator works, and the flow area decreases gradually with time. Therefore, the flow area within half a cycle is as follows, ignoring the influence of radial clearance flow:

$$S(t) \approx S_0 - 3\left(R_1^2 - R_3^2\right)\theta(t) = S_0 - 3\left(R_1^2 - R_3^2\right)\int_0^t \omega(t)dt \tag{9}$$

where $\omega(t)$ is the angel rotation velocity, rad/s. The upper-limit t is the duration of half a cycle.

At present, to generate a sinusoidal pressure wave, the motion mode of the rotor was wrongly designed as a sinusoidal function, as follows:

$$\omega(t) = \frac{(\varphi_H - \varphi_L)f\pi^2}{180}\sin(2\pi ft) \tag{10}$$

where φ_H, φ_L are the starting and stopping angles of rotor rotation, °; and f is the rotation frequency, Hz.

As shown in Fig. 3 (a) and (b), when the angular velocity changes sinusoidally with Eq. (10) mode, the rotation angle grows and decays sinusoidally, increasing from 0° to 28° and then reversing to 0°. However, the flow area has a linear relationship with the angle, but the pressure drop cannot keep the sinusoidal change, and there will be an uneven distribution of periods.

2.2. Defects and causes of waveform characteristics

Combined with Equations (1) and (6)~(10), the tool size and hydraulic parameters were substituted to calculate the theoretical pressure. The pulser type commonly used in the field is adopted. The outer diameter of the stator R_0 is 48.0 mm, which is 1 mm larger than the outer diameter of the rotor. It is used for annular gap flow. In addition, for ideal calculation, the medium is clean water and the displacement is normal working displacement, the specific parameters are shown in Table 1.

The pressure wave data of the simulation are compared with the standard sine wave, as shown in Fig. 4. Fig. 4 shows that the half-cycle time through the equilibrium position is unevenly distributed, and the ratio of the up half-cycle (T_{up}) to the down half-cycle (T_{down}) is 30%:70%. This defect of irregular period distribution seriously affects the power of the original signal downhole. It affects the quality and error rate of phase modulation and frequency modulation coding, which could be more conducive to the effective

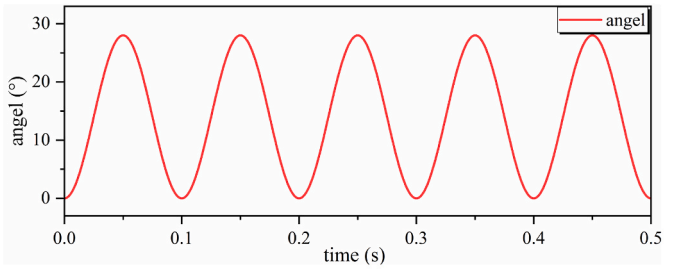

(a)

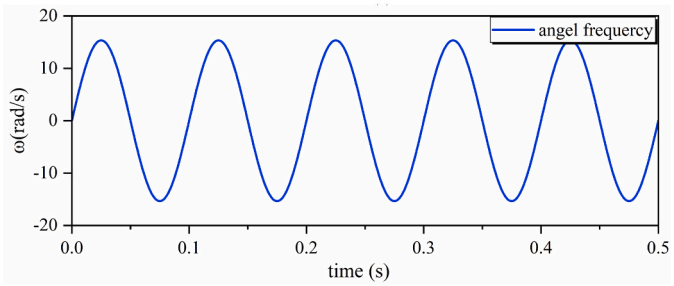

(b)

Fig. 3. The rotation angle velocity under the original condition (a), and The law of angle change under the original condition (b).

Table 1
Calculation parameters.

R_0 (mm)	R_1 (mm)	R_2 (mm)	R_3 (mm)	ρ_0 (kg/m^3)	Q (m^3/s)	C_d
48.0	47.0	22.0	16.5	998	0.045	0.65

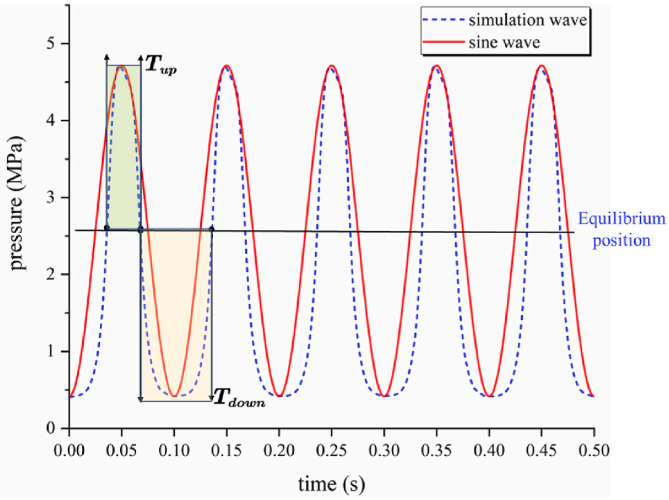

Fig. 4. Comparison diagram of the simulation wave and sine wave.

transmission of the signal.

To study the pressure change rate with time and angle. The ideal sinusoidal wave and the simulation pressure are differentiated in the time domain. As shown on the left of Fig. 5, the pressure change rate of the sinusoidal wave is also a sinusoidal law (red line), which is quite different from the simulated pressure wave (blue dashed line). The rotor rotates back and forth once for a cycle, divided into five stages. In stage OA, the rotor begins to accelerate and rotate to a certain angle, but the change in flow area is small, resulting in a pressure change rate less than ideal. When the rotor rotates in section AB, the pressure change rate increases rapidly. Then, when it reaches a certain angle, gap flow occurs between the rotor and stator, and the pressure change rate decreases rapidly to 0. In stage BC, the flow passage of the rotor moving backward is reopened, but the flow state is still kept around, so the pressure change is small. The pressures of stages CD and AB change similarly. As the opening angle of the flow passage increases to a certain angle, the flow disappears, and the pressure change decreases. In stage DE, the pressure change rate gradually decreases to 0, as in the OA stage, and a movement cycle is completed.

As shown on the right of Fig. 5, the pressure change rate of the sinusoidal wave varies with the angle into a perfect ellipse. In contrast, the pressure change rate of the simulated waveform presents a symmetric convex shape up and down. The process is the same as the above. One cycle is divided into five parts, but the corresponding angle range is refined. It is worth noting that the angles of the points in the first half of the cycle are slightly larger than those in the second half, probably due to the delay caused by the flow around

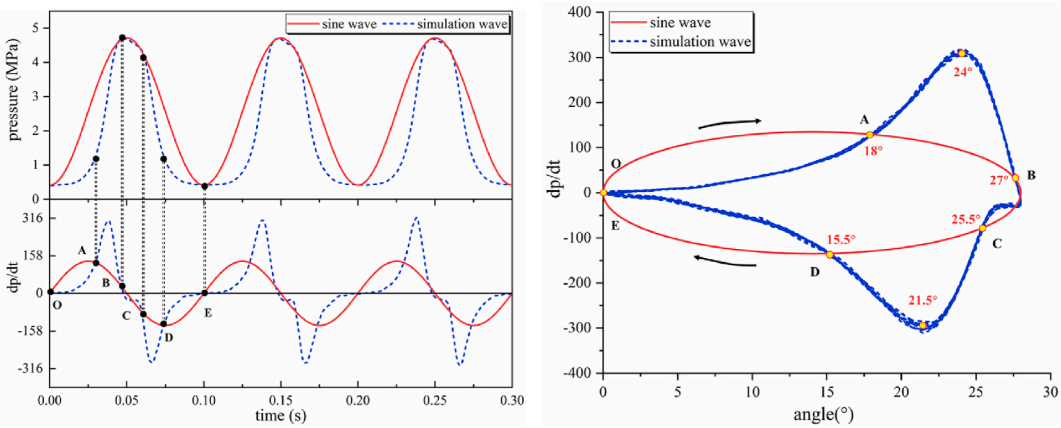

Fig. 5. The change in the pressure rate of a sine wave and simulation wave with time (left) and angle (right).

the fluid.

In conclusion, under the current mechanical structure and rotation mode, the pressure change rate of a small angle is less than that of large angles, resulting in the defect of uneven cycle distribution. In other words, the time of the rotor closing the runner is faster than that of opening the runner, so it needs to be adjusted and optimized. However, it is very difficult to solve the cycle allocation problem by mathematical derivation. It only needs to provide an adjustable parameter strategy in engineering. Therefore, waveform optimization design will be carried out from the field adjustable parameters.

2.3. Waveform optimization strategy

2.3.1. Optimization of the rotation angle range

Since the pressure change rate is small when the angle is small and large when the angle is large, the rotation's starting and stopping angles can be adjusted appropriately. Meanwhile, it is necessary to consider that the pressure wave amplitude will decrease accordingly when the total rotation angle is reduced. Therefore, angle optimization is needed to achieve a good sinusoid and high amplitude pressure wave signal. The angle control scheme carries out single factor control, in which starting and stopping angles are simulated. Then, the two parameters are optimized to select two groups of angles for simulation. The specific parameters are shown in Table 2.

2.3.2. Optimization of the rotation angular velocity mode

Optimizing the rotation angular velocity mode is necessary without adjusting the rotation angle range when considering the signal's amplitude. At present, a sinusoidal angular velocity motion model is adopted. However, the new motion mode needs to reduce the proportion time of small-angle motion and increase the proportion time of large-angle motion. Therefore, there are two ways to meet this requirement. First, the angular velocity of the rotation period is not changed, but the rotor stops at large angles. The angular velocity of the second rotation period is changed to achieve fast rotation at small angles and slow rotation at large angles. The former is called half-sine constant rotation, and the latter is called half-sine variable frequency rotation.

(1) Half-sine constant frequency rotation

In this way, the governing equations of angle and angular velocity are Eq. (11) and Eq. (12), as follows:

$$\theta_{hc} = \begin{cases} \dfrac{\theta}{2}[1-\cos(2\pi k_1 f t)] \ , \ 0 < t \le t_1 \\ \theta, t_1 < t \le t_2 \\ \dfrac{\theta}{2}[1-\cos(2\pi k_1 f(t-t_2)+\pi)], t_2 < t \le T \end{cases} \tag{11}$$

$$\omega_{hc} = \begin{cases} \pi\theta k_1 f \sin(2\pi k_1 f t) \ , \ 0 < t \le t_1 \\ 0, t_1 < t \le t_2 \\ -\pi\theta k_1 f \sin(2\pi k_1 f(t-t_2), t_2 < t \le T \end{cases} \tag{12}$$

where k_1 is an adjustable constant, $k_1 \ge 1$; $t_1 = 1/(2k_1 f) = T_k/2$, T_k is the period of frequency kf; $t_2 = T - T_k/2$, T denotes the original period.

When k_1 is 1.2, the angle and angular velocity comparison with the original ($k_1 = 1$) is shown in Fig. 6. When $k_1 = 1.2$, the rotation to the maximum angle stops, and then a plateau appears, which will enlarge the large-angle time of the waveform. Meanwhile, the angular velocity in the first half of the cycle is more significant than that in sine mode. The motor control difficulty is slightly more incredible than that in sine mode. However, the overall power is the same. The value of the constant k_1 will directly affect the pressure waveform characteristics, so the value range will be optimized to improve the waveform correlation and uniform waveform period distribution.

(2) Half-sine variable frequency rotation.

Similarly, a half-sine variable frequency rotation method was designed to compensate for the nonlinearity of the pressure-angle relation by using the angular velocity difference and improving the quality of the pressure waveform. The boundary angle of the

Table 2
The control scheme of the rotation angle.

Starting Angle θ_L	Stop Angle θ_H	$\theta_L \sim \theta_H$
0°~28°	0°–24°	9°–26°
6°–28°	0°–26°	9°–27°
9°–28°	**0°~28°**	12°–26°
12°–28°	0°–30°	12°–27°
15°–28°	0°–32°	

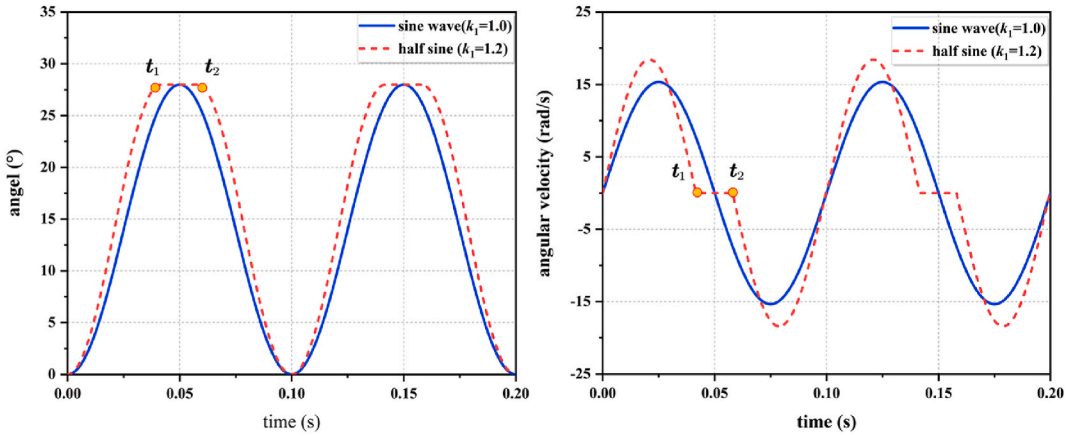

Fig. 6. Comparison of angle (left) and angular velocity (right) between half-sine rotation mode and sine rotation mode ($k_1 = 1.2, f = 10$ Hz).

upper and lower periods is set at 3/4 of the oscillating angle to simplify the governing Equation. The governing Equation is Eq. (13) and Eq. (14), as follows:

$$\theta_{hv} = \begin{cases} \beta_L + \dfrac{\varphi_H - \varphi_L}{2}\sin\left(2\pi f_k t - \dfrac{\pi}{2}\right), 0 < t \le t_1 \\ \beta_H + \dfrac{\varphi_H - \varphi_L}{2}\sin\left(2\pi f_p t - \dfrac{\pi}{3k_2 - 2}\right), t_1 < t \le t_2 \\ \beta_L + \dfrac{\varphi_H - \varphi_L}{2}\sin\left(2\pi f_k t - \dfrac{4k_2 - 3}{2}\pi\right), t_2 < t \le T \end{cases} \tag{13}$$

$$\omega_{hv} = \begin{cases} (\varphi_H - \varphi_L)\pi f_k \sin(2\pi f_k t), 0 < t \le t_1 \\ (\varphi_H - \varphi_L)\pi f_p \cos\left(2\pi f_p t - \dfrac{\pi}{3k_2 - 2}\right), t_1 < t \le t_2 \\ (\varphi_H - \varphi_L)\pi f_k \cos\left(2\pi f_k t - \dfrac{4k_2 - 3}{2}\pi\right), t_2 < t \le T \end{cases} \tag{14}$$

where , k_2 is a constant, $k_2 > \frac{4}{3}$; φ_L, φ_H denote the starting angle and stop angle, degrees; $\beta_L = \frac{\varphi_H - \varphi_L}{2}, \beta_H = \frac{\varphi_H + \varphi_L}{2}$, and β_H represent the boundary angle of the half period; $f_k = k_2 f > f$ is the frequency of the second half period, which is the frequency of the rotation angle between φ_L and β_H; and $f_p = \frac{3k_2}{2(3k_2 - 2)} f < f$ is the frequency of the first half period, which is the frequency of the rotation angle between β_H and φ_H. In addition, $t_1 = \frac{1}{3f_k}, t_2 = t_1 + \frac{1}{2f_p}$.

When k_2 is 1.5, the angle and angular velocity comparison with the original is shown in Fig. 7. As shown from the figure on the left, the change rate of the small angle in $0 \sim t_1$ is faster than that in sinusoidal mode when $k_2 = 1.5$. Moreover, the change rate of large

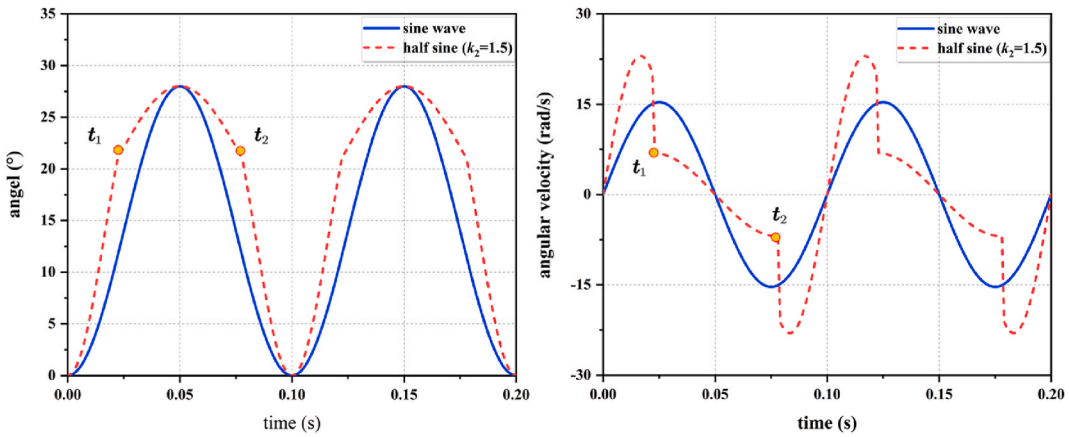

Fig. 7. Comparison of angle (left) and angular velocity (right) between half-sine rotation mode and sine rotation mode ($k_2 = 1.5, f = 10$ Hz)).

angles in $t_1 \sim t_2$ is less than that in sinusoidal mode, thus meeting the design requirements. In addition, it can be seen from Fig. 7. (right) that there is an apparent step phenomenon in angular velocity, which is caused by the frequency conversion under this control mode. This discontinuity of angular velocity increases the difficulty of motor control, but its average power is the same.

By integrating the above two half-sine control methods, the influence of constants k_1 and k_2 on the pressure waveform will be studied to determine the optimal value range. Its values are listed in Table 3.In summary, the pressure waveform can be optimized by controlling the motor's rotation angle and rotation mode. CFD numerical simulation was used to compare and analyze the results to verify the theoretical results.

3. CFD numerical simulation verification method

3.1. Grid model of the continuous wave generator

The structure of commercial continuous wave generator is complex, but its core components are stator and rotor, and the rotor is controlled by motor. As shown in Fig. 8, the stator and rotor are installed with a gap to prevent obstruction and tool damage when the pulser is completely closed. The stator and rotor have basically the same disc structure, this paper takes the 6-disc type as the research object. In addition, the radius of the rotor is 46.5 mm, the radius of the stator is 48 mm, and the gap size is 1.3 mm.

The flow channel is extracted based on the mechanical structure of the tool, and the geometric details that do not influence the signal are omitted. As shown in Fig. 9, the whole tool is 2.5 m in length and 100 mm in diameter. It is divided into 5 parts: the front section, stator, gap, rotor, and back section.

Considering that the turbulence characteristics at the gap are obvious when the tool is working, it is necessary to carry out local mesh encryption to capture the flow characteristics. At the same time, the structure of stator and rotor is complex, and the polyhedral mesh is used to divide the stator and rotor to ensure good wall adhesion. Based on the meshing strategy in the previous study [22], the gap and fixed rotor regions are locally encrypted and gradually sparse to both ends, as shown in Fig. 10.

3.2. Boundary conditions and parameters

As shown in Fig. 11, the boundary conditions are set according to the mud pulse generator's test conditions and software conditions. The actual ground drilling through the mud pump, generally the plunger pump, pumps into the drilling fluid. The quality of the drilling fluid can be controlled, so the inlet condition is chosen as the mass flow inlet. Meanwhile, the outlet condition is selected as a pressure outlet, set as 1 atm.

In addition, due to the complex composition of drilling fluids, there are no related materials in the software library. Meanwhile, to compare with future surface clean water experimental research, the numerical simulation uses clean water as the medium for simulation. Continuous wave generator generally operate at frequencies below 30 Hz, and 10 Hz was selected in this study. The displacement was set to 2.7 m^3/min according to the actual working condition of the tool.

Meanwhile, as the waveform characteristics of this model are consistent with those of the pipe model, the defects and causes of the short model can be analyzed to save some computing resources for later optimization. The reference calculation example of the digital modeling test is set as clockwise sinusoidal rotation, and the rotation angle is 0–28°. The Pearson coefficient is commonly used in mathematics to quantitatively study its correlation, which can express the similarity between simulated waveforms and sine waves [23], and the formula is Eq. (15):

$$\rho_{\Delta P,\Delta P_{\sin}} = \frac{\mathrm{cov}(\Delta P, \Delta P_{\sin})}{\sigma_{\Delta P}\sigma_{\Delta P_{\sin}}} \tag{15}$$

where $\rho_{\Delta P\ ,\ \Delta P_{\sin}}$ is the Pearson coefficient, the value of 1 means a complete positive correlation; $\Delta P, \Delta P_{\sin}$ represent the simulated pressure and the ideal sinusoidal pressure wave, MPa, respectively; and cov, σ are the covariance and standard deviation, respectively.

In addition, the standard sinusoidal pressure wave is Eq. (16):

$$\Delta P_{\sin} = \frac{\Delta P_{\max} - \Delta P_{\min}}{2}\sin(\omega t - \varphi_0) + \frac{\Delta P_{\max} + \Delta P_{\min}}{2} \tag{16}$$

where $\Delta P_{\max}, \Delta P_{\min}$ denotes the maximum and minimum pressure, MPa, and φ_0 is the initial phase angle, rad.

Table 3
Values of k_1 and k_2.

k_1	1	1.1	1.2	1.3	1.4	1.5
k_2	1.4	1.5	1.6	1.7	1.8	1.9

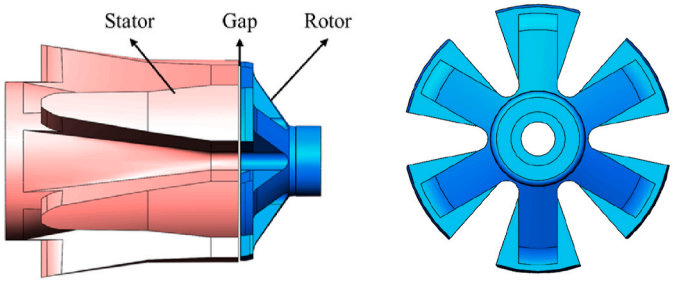

Fig. 8. Structure of the stator and rotor (left is the side view of the stator and rotor; right is the top view of the rotor).

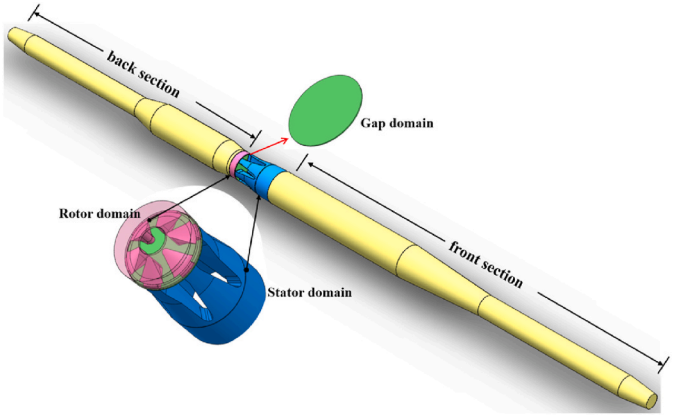

Fig. 9. The fluid domain of the continuous-wave mud pulse generator.

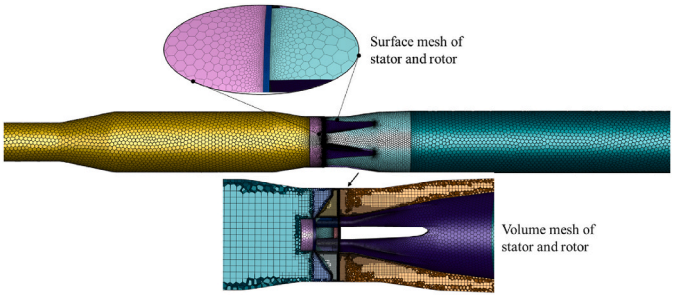

Fig. 10. The mesh of the mud pulse generator.

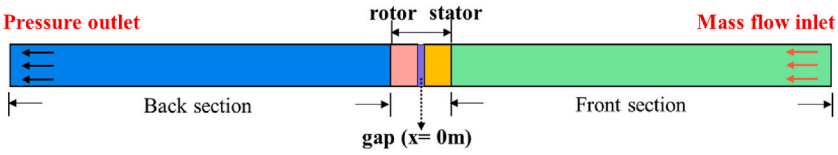

Fig. 11. The boundary conditions of inlet and outlet.

4. Results and analysis

4.1. CFD simulation verification

In Fig. 12, the pressure curve and pressure rate comparison is analyzed. First, the theoretical analysis and the CFD simulation method calculate the periodic pressure curve, and the time inequality is distributed, verifying the correctness of the theoretical

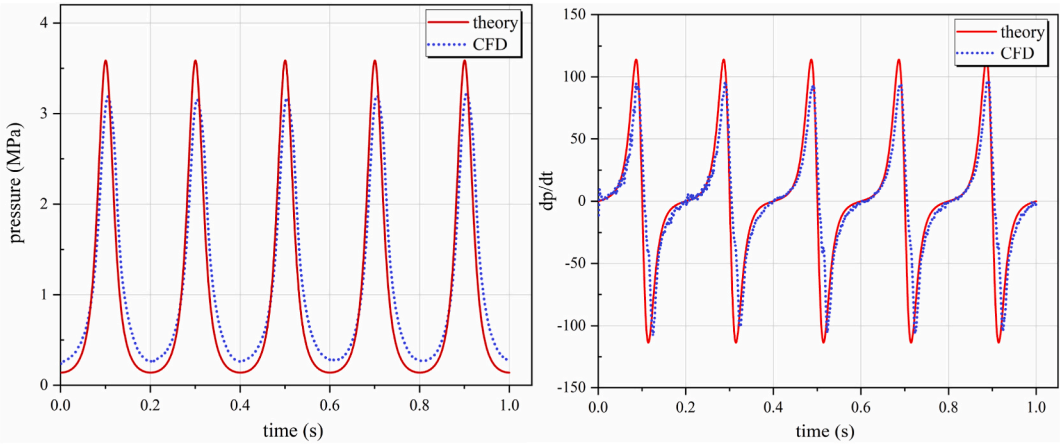

Fig. 12. Pressure (left) and pressure change rate (right) of theory and CFD simulation.

derivation. Meanwhile, the pressure change rate curve also represents the slow change of the small angle and the rapid change of the angle. The theoretical calculation of the pressure amplitude is slightly higher than the CFD because the theoretical derivation ignores the effect of the partisan gap and leads to the decrease of the flow area with the increase of the pressure amplitude. Because of the similarity of the simulation pressure waveform, the results are analyzed by the numerical simulation results of the system.

4.2. Starting angles and stop angles

The starting pressure and amplitude of the wave change with the difference in the starting and stopping angles. Meanwhile, the proportion time of the upper and lower half periods will change so that the waveform is closer to the ideal sine wave, and the power of the pressure wave will be improved.

4.2.1. Starting angle

The initial field pressure needs to be recalculated after the rotor is fixed at different initial angles, which results in different tool pressure drops at different initial angles. With the same stop angle ($\varphi_H = 28^\circ$), the upstream pressure varies with the starting angles, as shown in Fig. 13. It can be seen that with the increase in the starting angle, the trough of the wave increases gradually, while the peak of the wave remains unchanged, which will seriously affect the amplitude of the pressure wave. In addition, the lower half period of the pressure wave gradually decreases with increasing starting angle, so the uneven distribution of its period is improved. The figure on the right shows that the pressure change rate of small angles increases and gradually shifts to the ideal pressure wave. At the same time, the maximum pressure change rate decreases gradually, reducing the pressure transient variable, which ensures the control stability of the motor.

Three parameters must be considered comprehensively to improve the pressure wave shape, including the cycle distribution ratio (represented by the proportion of the above half-cycle time), pressure wave amplitude, and Pearson coefficient. The larger the amplitude of the pressure wave is, the higher the signal energy and the stronger the resistance to attenuation. Furthermore, the closer

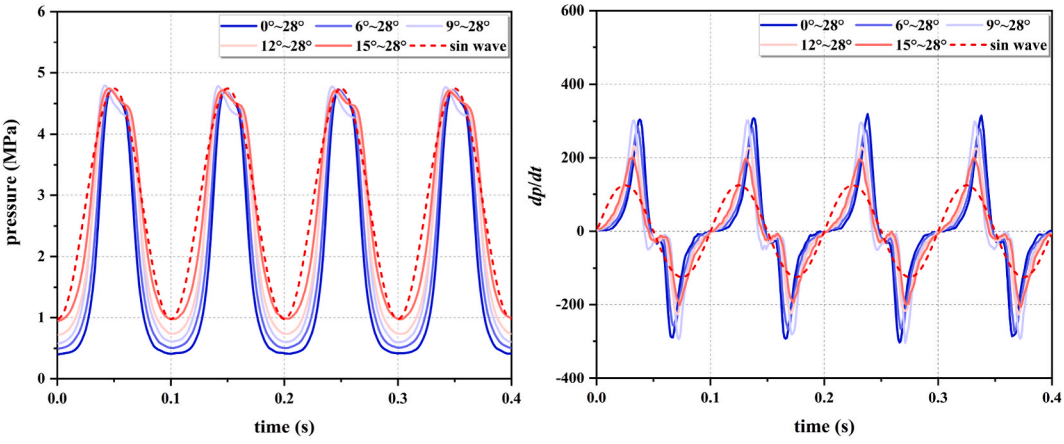

Fig. 13. Pressure (left) and pressure change rate (right) at different starting angles ($\varphi_H = 28^\circ$).

the time ratio is to 0.5, the better the sinusoid is. As shown in Fig. 14, pressure wave correlation and periodic distribution gradually improved with starting angles, while the pressure amplitude gradually decreased. Therefore, the three primary parameters do not change synchronously. It is appropriate to set the starting angle within the range of 9°–12°, considering the nonlinearity of the angle-pressure change rate.

4.2.2. Stop angles

The rotor is kept rotating from 0° ($\varphi_H = 0°$), Its stop angle gradually increases, leading to a decrease in the minimum flow area and changing the characteristics of pressure change at large angles. As shown in Fig. 15, the pressure wave peak gradually increases with increasing stop angles, and the pressure wave amplitude increases significantly. It is worth noting that the peak growth rate is minimal when the stop angles increase from 28° to 32°. That is because after the rotor is rotated to 28°, the axial flow area of the fixed rotor is 0 and no longer changes. At this time, there is more gap flow around, and its overflow pressure drop is stable. Similarly, it can be judged from the figure on the right that the pressure change rate of small angles increases with increasing stop angles. However, the extreme value of large angles also increases, which will increase the difficulty of motor control.

The pressure wave amplitude increases gradually and then remains constant, as shown in Fig. 16. The first half of the cycle time ratio and Pearson coefficient positively correlate with the stop angles. However, the time ratio is between 0.3 and 0.4, and the waveform needs to be significantly improved. Therefore, considering the waveform amplitude and motor control difficulty, the stop angle is selected as 26°–28°.

4.2.3. Starting angle with stop angles

It can be inferred from the studies in the first two sections that were increasing the starting angles, and the stopping angle simultaneously may be beneficial to waveform optimization. It can be inferred from the studies in the first two sections that the starting angle and the stop angle may increase simultaneously, which will be beneficial to waveform optimization. Therefore, four trials were selected based on the previous angle recommendations, as shown in Fig. 17. Smooth pressure wave curves are produced in the four groups of tests, and the peak position of the wave has no obvious distortion. At the same time, in the pressure change rate curve, only the 12–26° group had obvious steps in the decline stage of maximum change, while the other groups had smooth transitions. As shown in Fig. 18, when the starting angle is 9° and 12°, both the amplitude and correlation of pressure waves are higher in the former. In terms of the time ratio, the group of 9°–28° is the highest, and its waveform is closest to the sine wave. However, as the value points of the experiment are discrete and limited, more combination parameters are needed to optimize the angles accurately.

In conclusion, different starting angles and stop angles influence the waveform. As a relatively easy parameter to control in engineering, the specific value range of angles needs to be further studied. Other relevant factors, such as gap size and displacement, need to be considered.

4.3. Half sine control method

4.3.1. Half-sine constant frequency rotation

Keep the rotation angle from 0° to 28° and adjust the rotation mode to solve the pressure waveform problem. First, the rotation mode of half-sine constant frequency conversion is adopted. With the increase in k_1, the residence time of the rotor at 28° is longer, and the time of small-angle rotation is shorter. As shown in Fig. 19, a plateau region appears in the upper half of the pressure waveform, similar to a rectangular wave. The waveform of the second half period is still a smooth curve, but the time also decreases with increasing k_1. Meanwhile, it is observed that the maximum pressure change rate in the first half period increases with the increase in k_1

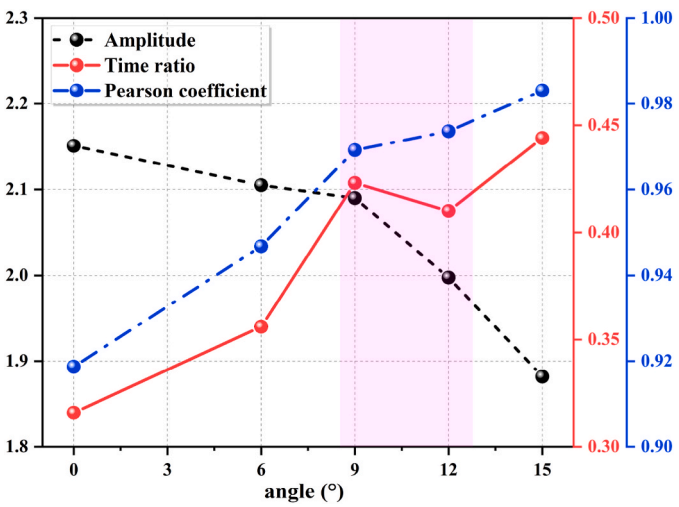

Fig. 14. The amplitude of the pressure wave, time ratio of the first half period, and Pearson coefficient change with the starting angles ($\varphi_H = 28°$).

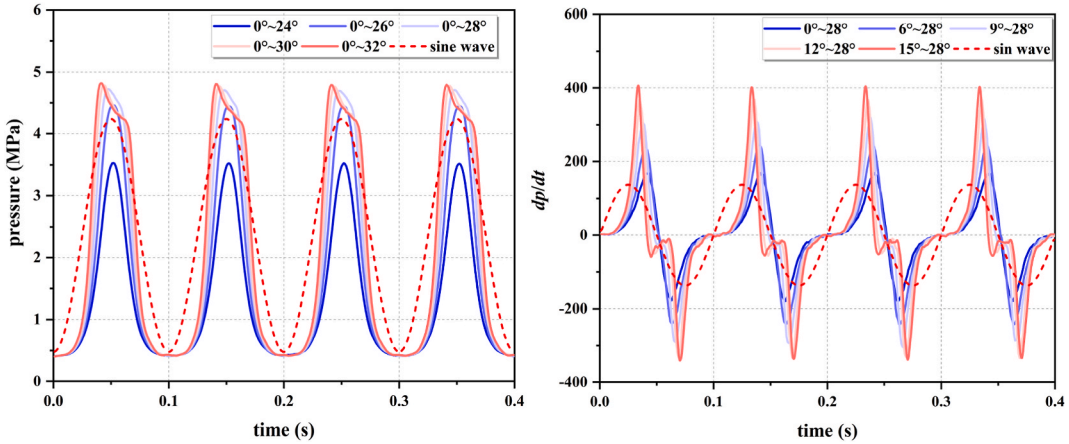

Fig. 15. Pressure (left) and pressure change rate (right) at different stop angles ($\varphi_H = 0^{\circ}$).

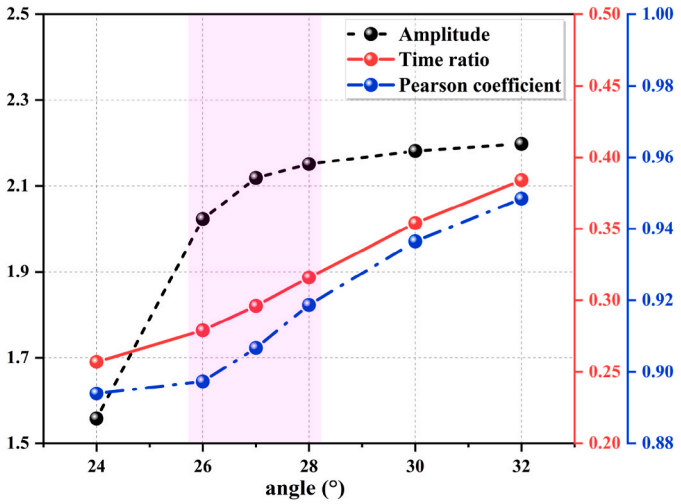

Fig. 16. The amplitude of the pressure wave, time ratio of the first half period, and Pearson coefficient change with the stop angles ($\varphi_L = 0^{\circ}$).

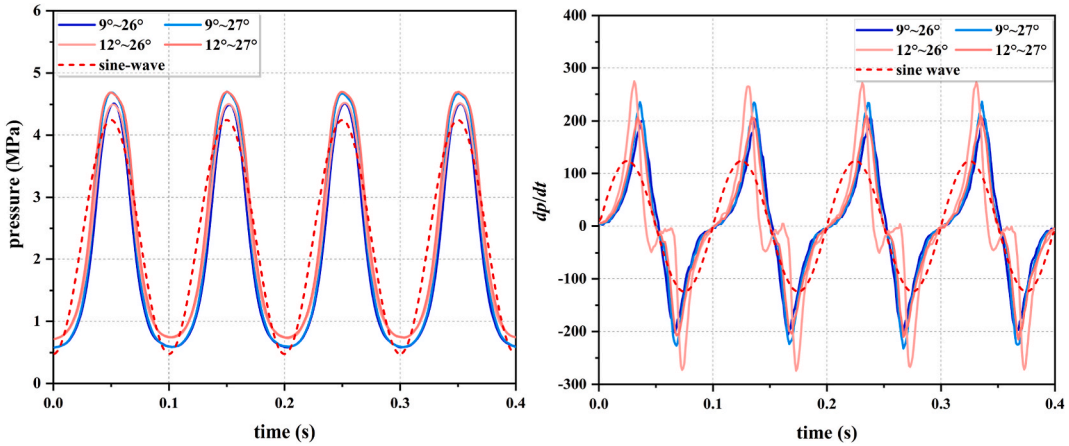

Fig. 17. Pressure (left) and pressure change rate (right) at different starting angles with stop angles.

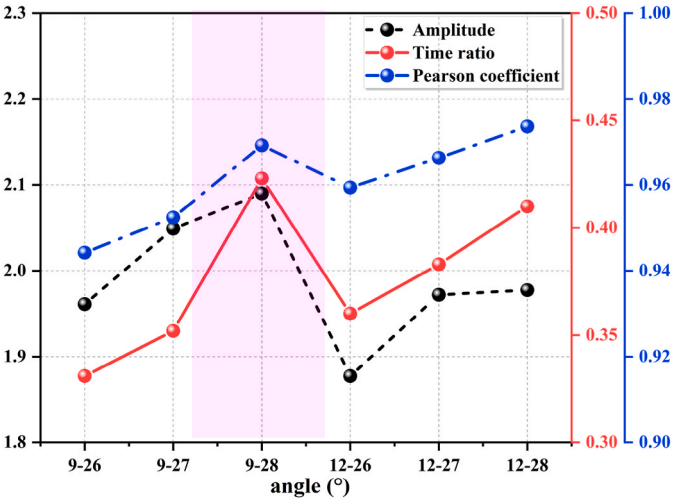

Fig. 18. The amplitude of the pressure wave, time ratio of the first half period, and Pearson coefficient change with the starting angles and stop angles.

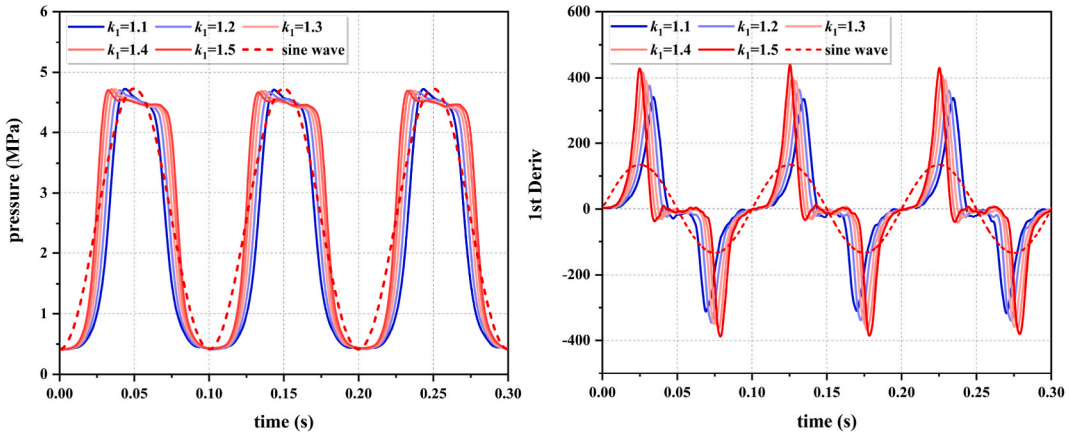

Fig. 19. Pressure (left) and pressure change rate (right) at half-sine constant frequency rotation mode.

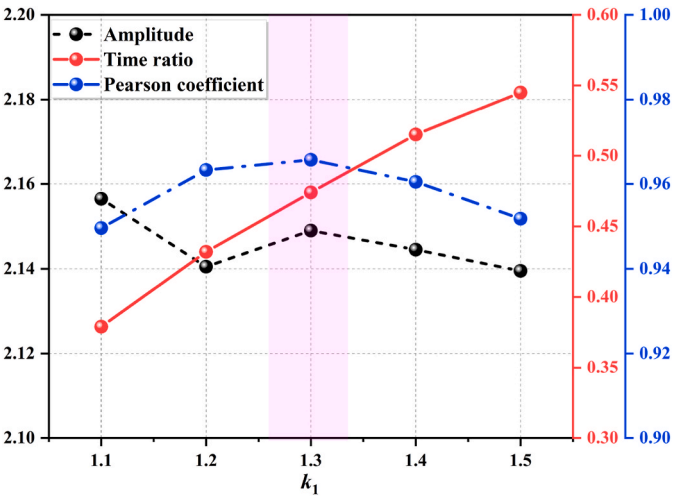

Fig. 20. The amplitude of the pressure wave, the time ratio of the first half period, and the Pearson coefficient change with k_1.

and moves to the left. The rotational angular velocity increases with k_1, and the rotor reaches 28° faster, causing greater pressure fluctuation.

As the rotation angle range remains unchanged, the amplitude of the pressure wave remains unchanged, as shown in Fig. 20. Meanwhile, the proportion of time in the first half of the cycle gradually increases. When k_1 is equal to 1.4, the time proportion exceeds 50%, which leads to uneven redistribution of waveform periods. The Pearson coefficient also reflects this, and the correlation of the pressure wave increases first and then decreases with increasing k_1. That indicates an optimal interval for the k_1 value, which makes the pressure cycle distribution close to the average. In this calculation example, a value of k_1 of approximately 1.3 can achieve this goal.

4.3.2. Half-sine variable frequency rotation

When the rotor adopts the half-sine variable frequency mode, the rotation frequency of the small-angle increases, and that of the large-angle decreases with the increase of k_2, which means that the small angle's rotation time is reduced. In contrast, the rotation time of the large angle is increased, thus solving the problem of uneven cycle distribution. As shown in Fig. 21, there is no obvious step change in the pressure curve, and it remains smooth, thus ensuring the concentration of signal energy. It can be seen that with the increase in k_2, both the upper and lower half periods of the pressure curve gradually approach the ideal sine wave, while the amplitude remains unchanged. At the same time, the pressure change rate curve shows that when k_2 increases, the maximum pressure change in the first half of the cycle gradually decreases and then gradually increases in the left shift. That may be because, with the increase in k_2, the frequency conversion angle gradually approaches the clearance flow position around the gap, which is related to the gap between the stator and rotor. In this experiment, k_2 is at the flow around the gap and occurs between 1.4 and 1.5, but when the gap changes, k_2 will also change.

Similarly, as shown in Fig. 22, the pressure wave amplitude does not change with k_2, while the time ratio increases approximately linearly. Although the correlation of the pressure wave gradually increases, its growth rate gradually slows down with k_2. When k_2 is greater than 1.5, its time ratio is less than 50%, not meeting the optimization requirements. Therefore, it is recommended that the value of k_2 be 1.6 in this experiment.

According to the above optimization control strategy and simulation results, the pressure waveform can be gradually sinusoidal by changing the rotor's rotation angle and rotation mode. However, the above simulation also has some defects and problems to be solved. First, the stator and rotor structures of the tool studied in this paper are specific, while other tool structures need to be calculated separately. Second, to save computing resources, the influence of upstream and downstream pipelines on the waveform is not considered in the numerical simulation. Relevant influence analysis will be carried out in our subsequent research. Then, the simulation uses clean water as the replacement for the drilling fluid, which is different from the actual situation and has a certain influence on waveform optimization. Nevertheless, this paper's research ideas and methods can provide a direction for pressure wave optimization to improve signal quality by integrating other optimization methods.

4.4. Defects and improvement suggestions for theories and CFD method

Given our previous continuous wave of wave studies [22], the numerical simulation results of the long pipeline simulated with the same parameters was compared and analyzed with the above model results. This long model firstly simulated the generation and transmission process of a downhole continuous wave signal. As shown in Fig. 23, the 1 m upstream and downstream pressures in the integrated generator and pipeline model were extracted for time-domain analysis, The upstream and downstream regions show periodic fluctuations, while the opposite phase is observed. During the first half cycle (0–0.05 s), it is generally accepted that upstream pressure increases gradually as the rotor closes the flow channel.

Meanwhile, the downstream pressure decreased simultaneously. The reason is that the pressure change detected by this long model

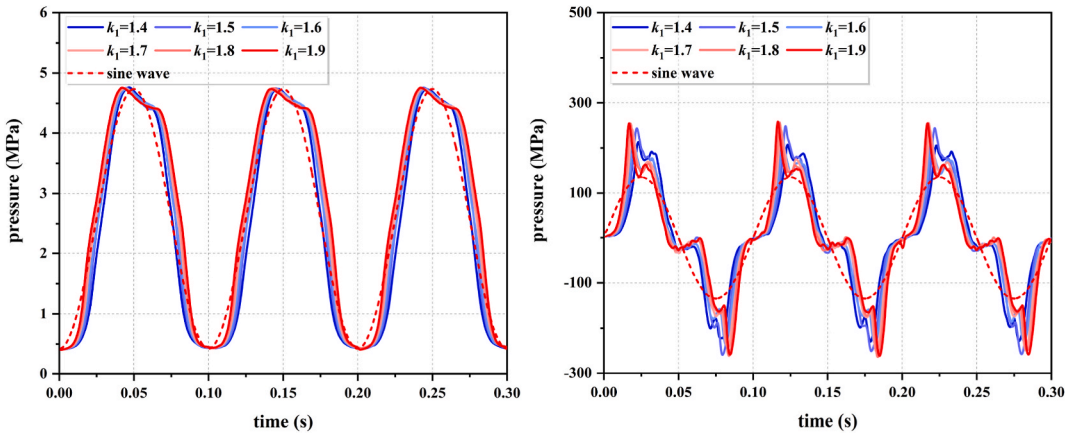

Fig. 21. Pressure (left) and pressure change rate (right) at half-sine variable frequency rotation mode.

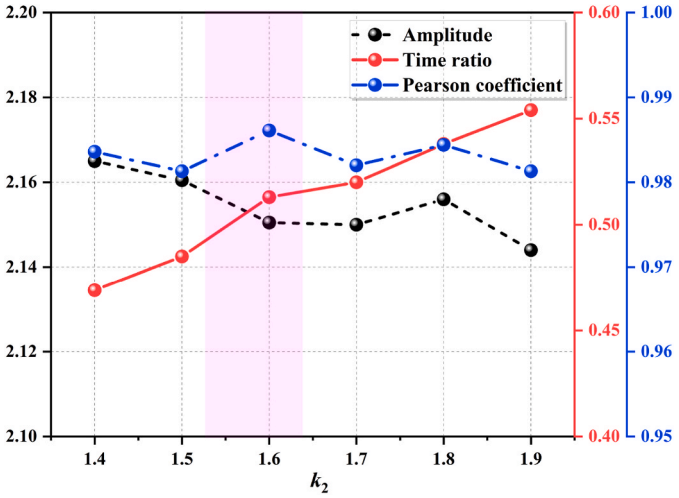

Fig. 22. The amplitude of the pressure wave, the time ratio of the first half period, and the Pearson coefficient change with k_2.

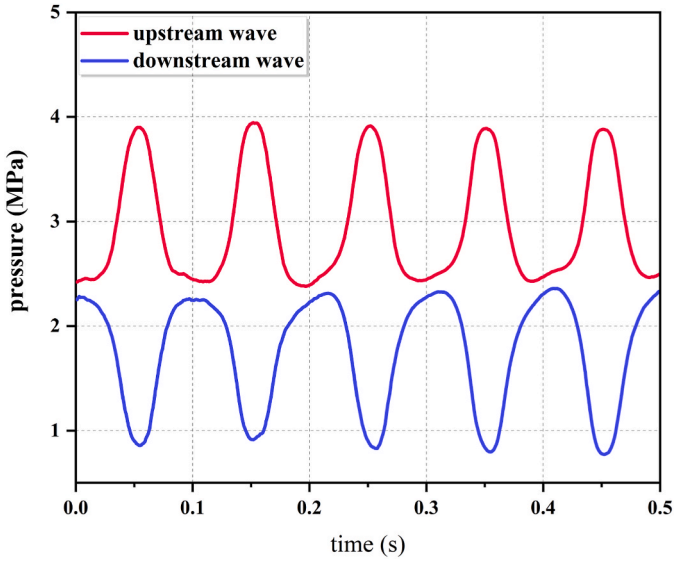

Fig. 23. Pressure wave when the frequency is 10 Hz (previous long model).

is not the change in the overcurrent pressure drop as previously known but the propagation of pressure waves. When the flow area decreases due to rotor closing, the flow of the upstream part near the rotor decreases, and the fluid particle far upstream moves downward at its original velocity, where the fluid is compressed, thus generating compression waves to transmit upstream. As the wavelength of 10 Hz is approximately 140 m, the pressure 1 m upstream is approximately the original waveform of the compression wave. In contrast, the fluid particles at the far end downstream of the rotor still move downward at the actual speed due to the decrease in the flow rate. The fluid density at the near end of the rotor decreases, and then the expansion wave is generated and propagates downstream.

In contrast to the thin-wall throttling theory and the CFD simulation of the continuous generator, it is assumed that the fluid density and flow rate through the tool does not change. Therefore, the pressure curve generated before is only the pressure difference across the tool, which is a hydrostatic drop, and it is not a pressure wave that can be propagated. However, the previous pressure waveform optimization work is useful. According to the basic theory of transient flow, the subtraction of upstream and downstream pressure waves is the tool pressure drop. As shown on the left of Fig. 24, the blue curve is the pressure drop curve after the pressure waves are subtracted (P_L), which shows periodic fluctuation. The red curve is the pressure drop curve of the theoretical model (P_S). The comparison period of the two models is the same, but there is a significant difference in amplitude. That is because the flow fluctuation cannot be generated in the simulation of the theoretical model, and the pressure drop is the overcurrent pressure drop under a constant flow rate. However, a flow wave is generated by transferring a pressure wave in actual conditions, so the tool pressure drop also

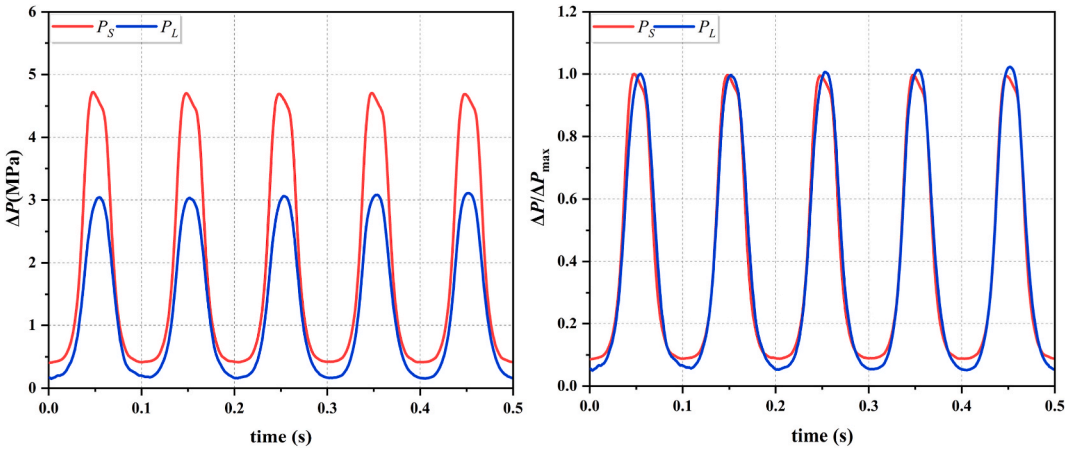

Fig. 24. Comparison of pressure drop under different models (left), comparison of pressure drop after homogenization (right).

fluctuates. Nevertheless, after homogenization, as shown on the right of Fig. 24, the correlation between the two reaches more than 99%, which shows that the differential pressure waveform of the theoretical model is consistent with the actual pressure waveform.

Since the pipeline model has many grids and a long calculation time, while the calculation time of the theoretical model and CFD model in this paper is fast, the sinusoidal preliminary optimization of the pressure waveform can be completed quickly. Our previous long pipeline model can determine the later pressure amplitude.

5. Conclusions

In this paper, a theoretical model of the oscillating shear valve type continuous wave generator was proposed to generating pressure. Given the poor sinusoidal characteristics of the pressure waveform, a detailed study is made from the theoretical derivation and pressure change rate-angle, and an optimization strategy is proposed. The optimization strategy adjusts the rotor rotation mode without changing the rotor structure, including the start-stop angle and the half-sine rotation scheme, and CFD numerical simulation method is used to verify.

The simulation results show that with increasing starting angles, the initial pressure increases, and the amplitude of the pressure wave decreases. However, the correlation between the pressure wave and the ideal sine wave increases gradually. Meanwhile, when the stop angle increases, the wave amplitude increases, and the correlation gradually increases. However, the pressure wave gradually appeared at a sharp angle in the first half of the period, where harmonic components increased. Therefore, it is recommended to choose an appropriate starting and ending angle range, which is 9°–28° in the model presented in this paper. In addition, the proposed two half-sine rotation methods both achieve the purpose of the sinusoidal pressure wave and do not increase the motor's power. The two strategies mentioned above can be coupled, and the specific parameters need further study. In a word, the research method in this paper provides a new set of numerical methods and ideas for sinusoidal continuous pressure waves, and there are still many problems worth studying in the future.

Declaration of competing interest

We declare that we have no financial and personal relationships with other people or organizations that can inappropriately influence our work, there is no professional or other personal interest of any nature or kind in any product, service and/or company that could be construed as influencing the position presented in, or the review of, the manuscript entitled.

Nomenclature

ρ_0	mud density (kg/m^3)
ω	rotation angular velocity (rad/s)
f	rotation frequency (Hz)
T	period (s)
R_0, R_1	the radius of stator and rotor (mm)
R_2, R_3	rotor characteristic radius (mm)
φ_L, φ_H	starting and stopping angles of rotor rotation (°)
$\Delta P, \Delta P_{\max}$	overcurrent pressure drop and peak pressure drop (MPa)
$\rho_{\Delta P, \Delta P_{\sin}}$	Pearson coefficient (−)
$\Delta P, \Delta P_{\sin}$	simulated pressure and the ideal sinusoidal pressure wave (MPa)

$\Delta P_{min}, \Delta P_{max}$	maximum and minimum pressure (MPa)
φ_0	initial phase angle (rad)
Q	displacement (m3/s)
C_d	flow coefficient (−)
S	flow area (m2)
θ	rotation angle (°)
θ_{hc}, ω_{hc}	rotation angle (°) and angular velocity (rad/s) of half-sine constant frequency
θ_{hv}, ω_{hv}	rotation angle (°) and angular velocity (rad/s) of half-sine variable frequency
f_k, f_p	frequency of the second half period and the second half period (Hz)
k_1, k_2	adjustable parameters in the control mode (−)Notes: In the nomenclature, the symbol "-" denotes dimensionless.

References

[1] S.J. Krase, P.R. Harvey, M.W. White, et al., A new measurement while drilling system designed specifically for drilling unconventional wells, in: The SPE/IADC Drilling Conference, 2013.
[2] X. Tang, Y. Zheng, V. Dubinsky, Logging while drilling acoustic measurement in unconsolidated slow formations, in: SPWLA 46th Annual Logging Symposium, 2005.
[3] R. Hutin, R.W. Tennent, S.V. Kashikar, New Mud Pulse Telemetry Techniques for Deepwater Applications and Improved Real-Time Data Capabilities, 2001.
[4] I. Wasserman, D. Hahn, D.H. Nguyen, et al., Mud-pulse telemetry sees step-change improvement with oscillating shear valves, Oil Gas J. 106 (24) (2008) 39–40.
[5] C. Klotz, A. Kaniappan, A.K. Thorsen, et al., A new mud pulse telemetry system reduces risks when drilling complex extended reach wells, in: The IADC/SPE Asia Pacific Drilling Technology Conference and Exhibition, 2008.
[6] C. Klotz, I. Wassermann, D. Hahn, Highly flexible mud-pulse telemetry: a new system, in: The SPE Indian Oil and Gas Technical Conference and Exhibition, 2008.
[7] A. Caruzo, R. Hutin, S. Reyes, et al., Advanced design and execution techniques for delivering high data rate MWD telemetry for ultradeep wells, in: The OTC Arctic Technology Conference, 2012.
[8] J. Fang, Z. Wang, P. Jia, et al., Model and characteristics analysis of downhole pressure signal generator with reciprocating fluid increasing valve, China Petrol. Mach. 44 (10) (2016) 11–16.
[9] M. Jia, Y. Geng, H. Yan, et al., Review of high-speed mud pulse telemetry technology, Chin. J. Sci. Instrum. 39 (12) (2018) 160–170.
[10] J.G. Proakis, M. Salehi, Digital communications, Digit. Commun. 73 (11) (2015) 3–5.
[11] J. Wu, R. Wang, Z. Rui, et al., Propagation model with multiboundary conditions for periodic mud pressure wave in long wellbore, Appl. Math. Model. 39 (23) (2015) 7643–7656.
[12] P. Wang, Y. Tian, J. Ji, et al., Topology optimization design for valve orifice shape of mud pulse generator based on continuous wave, J. China Univ. Petrol. 44 (5) (2020) 147–152.
[13] T.A. Seyler, M.M. Wisler, Adjustable Shear Valve Mud Pulser and Controls Therefor, Patent RE40944, USA, 2009.
[14] P. Jia, J. Fang, Y.N. Su, et al., Analysis on rotary valve hydraulic torque of drilling fluid continuous wave signal generator, J. China Univ. Petrol. 34 (1) (2010) 99–104.
[15] P. Jia, J. Fang, L.I. Lin, Optimization design of rotary valve of continuous wave generator based on correlation coefficient, Oil Field Equip. 41 (7) (2012) 37–42.
[16] M.A. Namuq, M. Reich, Laboratory experiments on pressure wave propagation in drill strings (mud pulse telemetry), Oil Gas Eur. Mag. 36 (3) (2010) 119–125.
[17] M.A. Namuq, M. Reich, Improving Mud siren (Continuous Wave) telemetry performance, in: SPE Offshore Europe Oil and Gas Conference and Exhibition, 2011.
[18] M.A. Namuq, M. Reich, A. Al-zoubi, Numerical simulation and modeling of a laboratory MWD mud siren pressure pulse propagation in fluid filled pipe, Oil Gas Eur. Mag. 38 (3) (2012) 125–130.
[19] C. Wei, Z. Yan, J. Shao, et al., Design of a rotary valve orifice for a continuous wave mud pulse generator, Precis. Eng. (2015) 111–118.
[20] J. Wu, R. Zhang, R. Wang, Mathematical model and optimum design approach of sinusoidal pressure wave generator for downhole drilling tool, Appl. Math. Model. 47 (2017) 587–599.
[21] Z. Yan, Y. Geng, C. Wei, et al., Design of a continuous wave mud pulse generator for data transmission by fluid pressure fluctuation, Flow Meas. Instrum. 59 (2017) 28–36.
[22] H. Han, L. Xue, H. Fan, et al., Analysis of pressure wave signal generation in Mpt: an integrated model and numerical simulation approach, J. Petrol. Sci. Eng. 209 (2022), 109871.
[23] Z. Wang, D. Gao, J. Fang, et al., Optimal design and experimental modification of multirow valve ports generating drilling fluid continuous wave, Arabian J. Sci. Eng. 44 (6) (2019) 6067–6077.